2D Materials

OPEN ACCESS

RECEIVED
24 February 2021

REVISED
1 April 2021

ACCEPTED FOR PUBLICATION
19 April 2021

PUBLISHED
5 May 2021

PAPER

Moiré phonons in twisted $MoSe_2$–WSe_2 heterobilayers and their correlation with interlayer excitons

Philipp Parzefall[1,5], Johannes Holler[1,5], Marten Scheuck[1], Andreas Beer[1], Kai-Qiang Lin[1], Bo Peng[2], Bartomeu Monserrat[2,3], Philipp Nagler[1], Michael Kempf[4], Tobias Korn[4] and Christian Schüller[1,*]

[1] Institut für Experimentelle und Angewandte Physik, Universität Regensburg, 93053 Regensburg, Germany
[2] Theory of Condensed Matter Group, Cavendish Laboratory, University of Cambridge, Cambridge CB3 0HE, United Kingdom
[3] Department of Materials Science and Metallurgy, University of Cambridge, Cambridge CB3 0FS, United Kingdom
[4] Institut für Physik, Universität Rostock, 10059 Rostock, Germany
[5] These authors contributed equally.
[*] Author to whom any correspondence should be addressed.

E-mail: christian.schueller@ur.de

Keywords: moiré phonons, moiré superlattice, Raman scattering, transition-metal dichalcogenides, interlayer excitons

Abstract

We report about the investigation of twisted $MoSe_2$ homo- and $MoSe_2$–WSe_2 heterobilayers by means of low-frequency Raman spectroscopy (LFRS) and low-temperature micro photoluminescence (μPL). In room-temperature LFRS experiments on both, twisted $MoSe_2$ homobilayers and twisted $MoSe_2$–WSe_2 heterobilayers, we observe moiré phonons, i.e. folded acoustic phonon modes due to the moiré superlattice. In the heterobilayers, we can identify moiré phonons of both materials, $MoSe_2$ and WSe_2. While the twist angles for the homobilayers are relatively precisely known from the applied tear-and-stack preparation method, the twist angles of the heterobilayers have to be determined via second-harmonic-generation microscopy on monolayer regions of the samples, which has significant uncertainties. We show that by the moiré phonons of the heterobilayers, the relative twist angles can be determined on a local scale with much higher precision. We apply our technique for the investigation of a large area H-type (twist angle $\theta = 60° + \delta$) $MoSe_2$–WSe_2 heterobilayer. These investigations show that spatial regions, which can be identified to be atomically reconstructed (i.e. $\delta = 0°$) by the observation of an interlayer shear mode in LFRS experiments, exhibit a strong, momentum-allowed interlayer-exciton signal in low-temperature μPL. On the contrary, regions, where moiré phonons are observed, i.e. which can be identified to be rigidly twisted by a misalignment angle in the range of $5° \lesssim |\delta| \lesssim 6°$, exhibit no significant interlayer-exciton signals.

1. Introduction

One of the most fascinating properties of van der Waals materials is the possibility to stack different materials on top of each other with arbitrary, but well-controlled relative crystal orientations [1]. For bilayer graphene this has, e.g. lead to the intriguing discovery of a superconducting state [2]. Within the tremendous number of van der Waals materials which nature offers, the semiconducting transition-metal dichalcogenides (TMDCs) have attracted a lot of attention during the past decade [3, 4]. A foremost reason for this is that they represent in the monolayer form direct-bandgap semiconductors [5]. Superior properties of these materials are huge exciton binding energies [6], accompanied by large oscillator strengths [7], and, as a combination of noninversion symmetry and a strong spin-orbit interaction, the so called spin-valley locking [8, 9]. In the past few years heterobilayer structures, like $MoSe_2$–WSe_2 heterobilayers, which exhibit a staggered type-II band-edge alignment [10–12] have been in the focus within this research avenue. In these structures, an ultrafast charge separation of photoexcited charge carriers into the two constituent layers takes place, and interlayer excitons (ILEs) form [13–16]. For the $MoSe_2$–WSe_2 system, the ILE are momentum-allowed—i.e. optically bright—only,

if the two constituent layers are crystallographically aligned [17]. This means, rotated by $\theta = 60°$ (H-type stacked) or by $\theta = 0°$ (R-type stacked) relative to each other. The research on TMDC bilayers has been recently strongly driven by the fact that in twisted bilayers moiré superlattices can form. The effects of moiré superlattices on ILE in heterobilayer structures has fueled this research strongly [18–25]. Moreover, the long-range periodicity, arising from the moiré potential landscape, can enable fundamental changes of the electronic and phononic properties of van der Waals homo- and heterostructures [2, 26–31]. For rigid lattices, moiré structures are expected to form in heterobilayers even for perfectly aligned structures, because of the different lattice constants of the constituent materials [32]. However, this would only be true, if it would also be the energetically most favorable state. Indeed, very recently it has been shown experimentally via conductive atomic force microscopy [33] and transmission electron microscopy [34] that in TMDC heterobilayers [33, 34] and homobilayers [34] for small twist angle deviations δ from $\theta = 0° + \delta$ or $\theta = 60° + \delta$, atomic reconstruction takes place, where the atoms in the two constituent layers arrange like in R- or H-type homobilayers. Similar reconstructions have also been reported for bilayer graphene [35]. In [33, 34] it is shown that in the bilayers domains with H-type or R-type stacking configurations form, where the size of the domains depends on the twist-angle deviation δ. The range here is from several tens to one hundred nanometers [33]. The domain formation was first predicted in [36], and confirmed by density functional theory calculations [33, 34, 37, 38], and by a classical modelling [31]. Interestingly, in atomically-reconstructed structures the domain periodicity depends in the same way on the twist-angle deviation, as the moiré periodicity in structures, where the twist angle is larger than the critical value for atomic reconstruction [37]. Hence, a noninvasive and simple method, by which samples can be characterized on a local scale with regard to atomic reconstruction and/or a precise determination of the local twist angle, i.e. the moiré periodicity, is highly desireable.

From the beginning, Raman spectroscopy has been a powerful tool for the investigation of two-dimensional crystals. It has been very successfully applied to graphene [39] and to TMDCs, see, e.g. the review articles [40–42], and references therein. Raman spectroscopy can also play a pivotal role for the characterization and investigation of moiré superlattices. This has been impressively demonstrated by the work of Lin *et al* [43], where the first observation of folded acoustic and optical phonons due to the moiré super-Brillouin zone, is reported for twisted MoS_2 homobilayers. There, the name moiré phonons was coined for the backfolded modes, which we also use here. Recently, moiré phonons were also detected and systematically studied in WSe_2 twisted homobilayers [44]. So far, LFRS on interlayer shear- (ISM) and breathing modes (BMs) has been an important tool for the investigation of interlayer coupling in bilayer- and multilayer structures. In [45] a bond polarizability model is introduced to describe how the LFRS intensities depend on the stacking sequence of different 2D materials. The first observation of ISM, where adjacent layers oscillate rigidly against each other, in MoS_2 multilayers was reported by Plechinger *et al* [46]. Crucially, for the existence of ISM, a restoring force for the rigid layer displacement is required, which is always present in naturally stacked (3R or 2H) multilayers of the same material, due to the atomic registry between the layers. Subsequently, ISM have also been observed for other TMDC multilayers and homobilayers with R-type or H-type stackings [43, 47, 48]. For twist angles θ other than 0° or 60° [43, 48], or, for heterobilayers [47] and hetero-multilayers [49], where there is no restoring force for an ISM expected under the assumption of rigid lattices, only BM were reported [43, 47–49]. For the BM, the van der Waals force between the layers plays the role of the restoring force. In [48] it is shown how the BM can be used to identify regions of different high-symmetry stackings in slightly twisted homobilayers. The first observation of an ISM in $MoSe_2$–WSe_2 heterobilayers has been reported in [17], and for MoS_2–WS_2 heterobilayers in [50]. In a recent work on $MoSe_2$–WSe_2 heterobilayers [51] it was shown that via observation of an ISM, regions of atomic reconstruction can be detected for twist-angle deviations of $|\delta| < 4°$, i.e. in this twist-angle range there are domains with perfect R-type or H-type stackings of the heterobilayers. This is due to the fact that a finite restoring force for the shear motion is only present, if there is an atomic registry between the two layers, i.e. if they are stacked with exact R-type or H-type alignment. Atomic reconstruction for $|\delta| \lesssim 4°$ was confirmed recently also for WSe_2 homobilayers [44]. There, it was found that for $|\delta| > 4°$, where moiré superlattices form, the moiré phonons and in particular the BM can be used as sensitive probes of the local twist angle in large-scale Raman hyperspectral imaging experiments. An important result of this study was that the twist angle varies locally by about one degree on the scale of a few micrometers. This happens most likely due to imperfections, occurring in the stamping process of the bilayers.

In the present work we have prepared large series of $MoSe_2$ homobilayer and $MoSe_2$–WSe_2 heterobilayer samples via mechanical exfoliation and deterministic dry transfer. For the $MoSe_2$ homobilayers we report the observation of moiré phonons for twist-angle deviations $|\delta| > 4°$. Via samples with different twist angles, which are prepared by the tear-and-stack technique (see section 2) and, therefore, the twist angles are very accurately known, we

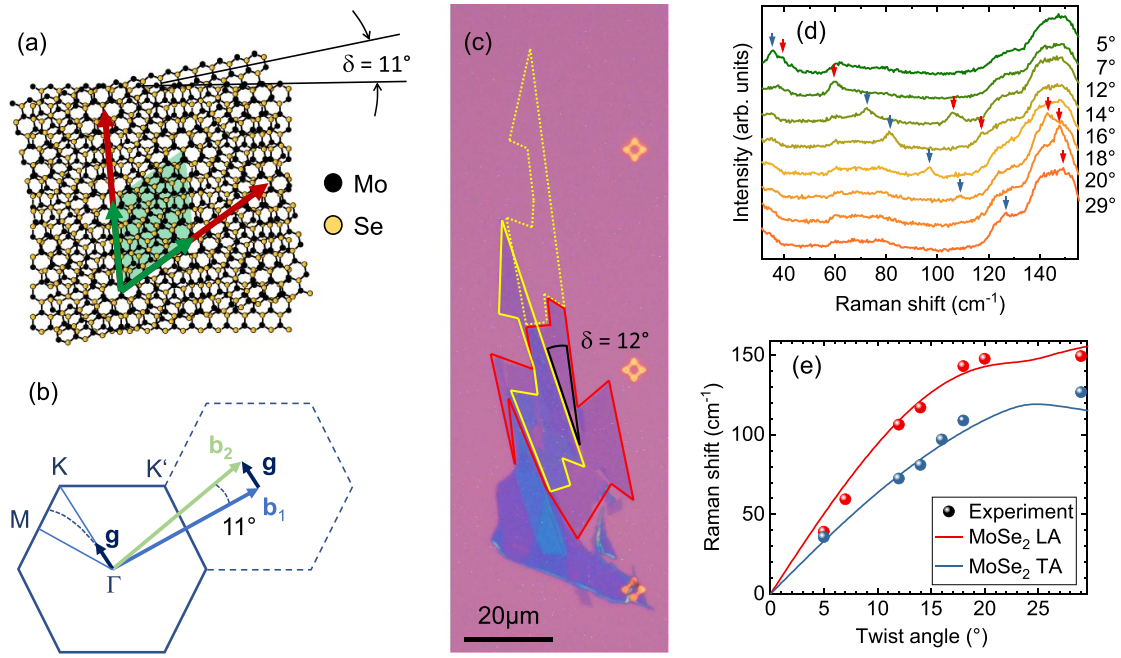

Figure 1. (a) Schematic picture of a twisted $MoSe_2$ homobilayer. The moiré superlattice vectors and primitive unit cell are shown by green arrows and a green-shaded region, respectively. The red arrows indicate the lattice vectors of the crystallographic superlattice. (b) First Brillouin zone and a neighboring Brillouin zone of one of the layers. $\mathbf{b}_1$ and $\mathbf{b}_2$ are reciprocal lattice vectors of the two twisted lattices. $\mathbf{g}$ is a reciprocal lattice vector of the moiré superlattice. (c) Microscope image of a twisted $MoSe_2$ homobilayer sample, which is prepared by the tear-and-stack technique. The yellow dotted line indicates the position of the top layer before it was torn off. (d) Stokes LFRS spectra of a series of twisted $MoSe_2$ homobilayers. The twist angles, as intended in the preparation process, are indicated. The arrows mark peaks, which are identified as moiré phonons. (e) Comparison of experimentally determined mode positions and calculated LA and TA phonon dispersions of a $MoSe_2$ monolayer.

demonstrate good agreement of the energies of folded acoustic phonons with the monolayer phonon dispersion. The latter are calculated via the supercell approach, with the real-space force-constants calculated in the density-functional perturbation theory [52]. The main focus of the present work, however, is the observation of moiré phonons in twisted $MoSe_2$–WSe_2 *hetero*bilayers. In some of these samples, folded acoustic modes of *both* constituents can be observed. We show that the moiré phonons allow for a much better local twist-angle determination, as compared to angle-resolved second-harmonic (SHG) microscopy, on which one otherwise has to rely for heterobilayer samples. We then apply our technique to the investigation of a large-area H-type heterobilayer sample, for which—from SHG—a twist-angle deviation of $|\delta| = (5 \pm 3)^\circ$ is determined. We show that by LFRS experiments we can identify sample regions, which show a strong ISM and no moiré phonons, i.e. which are obviously atomically reconstructed. In these regions, a strong interlayer exciton peak is observed in low-temperature μPL. In the major part of the sample, however, no ISM but moiré phonons can be found, from which a finite, local twist-angle variation between about 5° and 6° can be concluded. In these regions, no, or only weak signals from interlayer excitons are detected.

2. Materials and methods

2.1. Sample preparation

All homo- and heterobilayer samples are prepared on silicon wafers with a SiO_2 layer via mechanical exfoliation, using Nitto tape, and a deterministic all-dry transfer technique [53], employing polydimethylsiloxane (PDMS) stamps. After preparation, all samples are annealed in vacuum at a temperature of ~ 400 K for at least one hour to reach tight contact between the constituent layers. For the preparation of twisted $MoSe_2$ bilayers, a special procedure is used, which we will call in the following *tear-and-stack*, and which is motivated by a previously developed method [54]. First, a large-area $MoSe_2$ monolayer is partially stamped by the PDMS film onto the SiO_2 wafer. The PDMS stamp is then abruptly lifted again so that the $MoSe_2$ monolayer is torn in half and one part sticks on the SiO_2 wafer, while a second part still sticks on the PDMS film. The SiO_2 wafer is then rotated by a defined angle and subsequently the layer on the PDMS film is stamped onto the first layer. Via this procedure, the twist angle is relatively accurately known. Figure 1(c) shows a microscope image of one of the bare homobilayer samples, prepared by the described tear-and-stack technique. $MoSe_2$–WSe_2 heterobilayers are fabricated by two sequential

stamping processes of the two constituent layers. Here, straight edges of the individual flakes are used as an orientation for estimates of the twist angle.

2.2. Optical experiments

The twist angles of all heterobilayer samples are determined via angle-resolved SHG microscopy [55]. The uncertainties associated to this method are elaborated in more detail in the main body of the paper. For the SHG experiments, a mode-locked Ti:Sapphire laser is used at ~ 800 nm wavelength and with ~ 100 fs pulses. The co-polarized SHG signal is analyzed with a rotatable half-wave plate and a linear polarizer, and detected in a grating spectrometer with Peltier-cooled CCD camera. The Raman and μPL experiments are performed in an optical scanning-microscope setup. LFRS spectra are taken at room temperature under ambient conditions, while the μPL spectra are conducted in a cold-finger cryostat at nominally $T = 4$ K. As excitation source for both types of experiments, a 532 nm laser line is used. The laser is focused to a spot of ~ 1 μm diameter by a $100\times$ microscope objective. For stray-light reduction in the LFRS experiments, we use a Bragg-filter set. The spectra are analyzed with a grating spectrometer and a Peltier-cooled CCD camera.

3. Results and discussion

We start our report by the investigation of $MoSe_2$ homobilayer samples. The moiré-lattice formation in homobilayers and its characteristics are nicely described in the excellent work on MoS_2 homobilayers by Lin *et al* [43] (cf also [56] on twisted bilayer graphene). We start here with a very brief description of the most important features. Figure 1(a) shows a schematic picture of a twisted R-type ($\theta = 0°$) homobilayer in real space with a twist-angle deviation of $\delta = 11°$. The moiré-pattern formation can be seen, and the corresponding moiré lattice vectors and the resulting supercell are indicated by green arrows and a green-shaded region, respectively. The lattice vectors of the crystallographic superlattice, which for $\delta = 11°$ is a (7,5) superlattice [43, 56], are also indicated by red arrows. They are for this case just twice as long as the moiré lattice vectors. Figure 1(b) shows the first Brillouin zone of one of the layers and a corresponding reciprocal lattice vector $\mathbf{b}_1$. The reciprocal lattice vector $\mathbf{b}_2$ of the twisted lattice is also shown. The reciprocal lattice vector of the moiré superlattice is then given by $\mathbf{g} = \mathbf{b}_2 - \mathbf{b}_1$. The dotted line from the Γ point of the first Brillouin zone to the middle between the M and the K point indicates schematically the curvature, which is followed by $\mathbf{g}$ for larger twist angles $\delta \leqslant 30°$. For Raman scattering, energy and momentum conservation holds. In a translationally-invariant crystal, the momentum conservation reads

$$\mathbf{k}_s = \mathbf{k}_i \pm \mathbf{q} + \mathbf{G}, \qquad (1)$$

where $\mathbf{k}_i$ ($\mathbf{k}_s$) is the wave vector of the incident (scattered) light and $\mathbf{q}$ that of the created/annihilated (plus/minus sign) phonon in the crystal. Since $\mathbf{k}_i \sim \mathbf{k}_s \sim 0$ in the visible spectral range, when compared to the extension of the Brillouin zone, we have $\mathbf{q} \sim \pm\mathbf{G}$ for the wave vector of the phonon. $\mathbf{G}$ is a reciprocal lattice vector, which does not play a significant role in a usual crystal without superlattice, since all higher Brillouin zones can be projected to the first Brillouin zone, and therefore $\mathbf{q} \simeq 0$ holds for the momentum of the phonons, observable in a Raman experiment. Now the moiré superlattice comes into play. If we use the reciprocal lattice vector $\mathbf{g}$ of the moiré superlattice in equation (1) for $\mathbf{G}$, it follows that, e.g. acoustic phonons, which are usually inaccessible in Raman experiments due to the small momentum of visible light, can be expected in LFRS experiments on twisted bilayer samples. They can be mapped out by the reciprocal superlattice vector $\mathbf{g}$. This phenomenon is well known from one-dimensional short-period semiconductor superlattices (e.g. GaAs–AlAs), and the mapped phonons are then also called folded acoustic phonons. In [43] and [44] it was found that it is the moiré reciprocal lattice vector $\mathbf{g}$ rather than the reciprocal lattice vector of the crystallographic superlattice, which contributes to the Raman scattering in the accessible frequency range. Moreover, a crystallographic superlattice occurs for distinct commensurate lattice arrangements, i.e. distinct twist angles, only [43, 56]. Therefore, we will use the moiré reciprocal lattice vector in the following. It is important to note here that the assumption of zone folding is only approximately correct. Very recently, it has been shown for twisted bilayer graphene [57] and MoS_2 [58] that interlayer coupling and lattice reconstruction can lead to frequency renormalizations and even sidebands [57] of phonons.

Figure 1(c) shows a microscope image of one of the $MoSe_2$ homobilayers, which is prepared by the tear-and-stack technique. The bottom layer is outlined by a red line, while the top layer is marked by a yellow line. The position, where the top layer was torn off before, is outlined by a yellow dotted line. From this preparation procedure, the twist angle is relatively accurately known. By hyperspectral imaging of this sample (not shown), we determine, similar to the results of [44] on WSe_2 homobilayers, a local variation of the twist angle across the bilayer region of about 1°. We have prepared in total about 15 homobilayer samples by this technique. For samples with twist-angle deviations $|\delta| \leqslant 5°$ (not shown), we find a pronounced ISM mode, which is an indication for atomic reconstruction (R-type) [51]. In eight samples with twist-angle deviations $|\delta| \geqslant 5°$, clear indications for moiré phonons can be found. In figure 1(d), Stokes Raman spectra for these eight samples with twist angles between 5° and 29° are shown in the frequency region, where the folded acoustic phonon modes appear, which is above the low-frequency region of

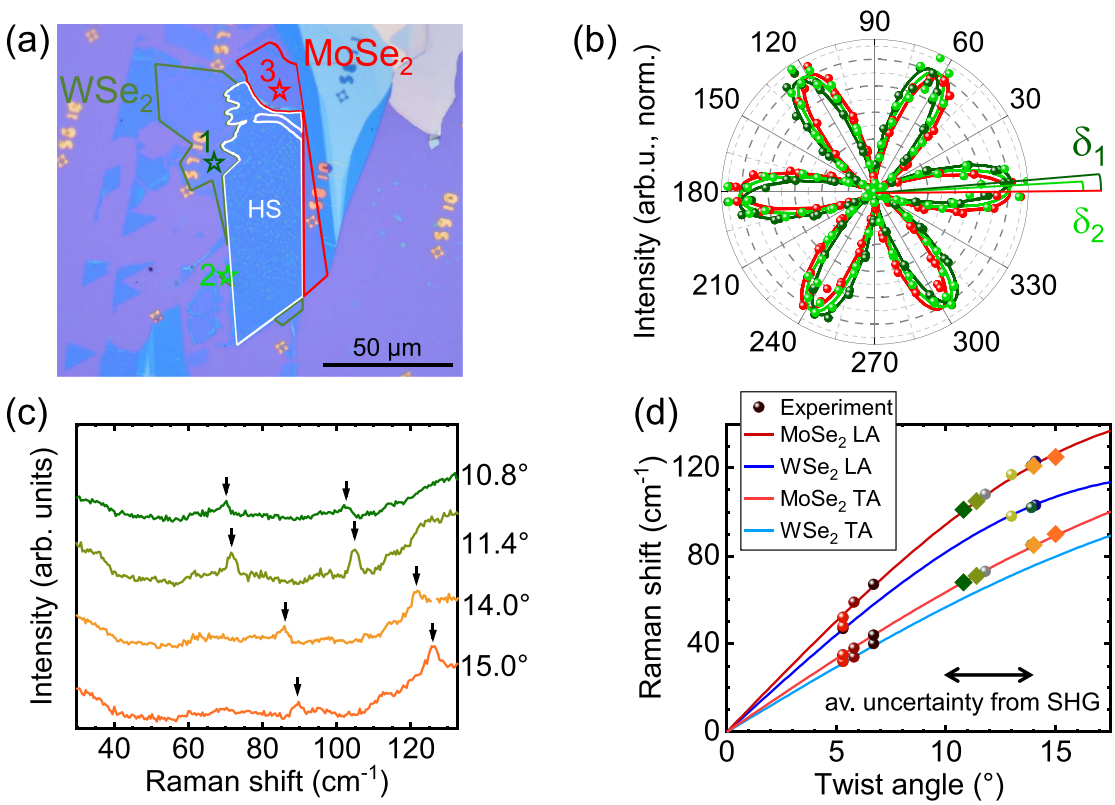

Figure 2. (a) Microscope image of a $MoSe_2$–WSe_2 heterobilayer. The heterostructure region is marked by a white solid line. At the three positions, marked by colored stars, SHG measurements on the monolayers are taken. (b) Polar plot of the angle-resolved, normalized SHG intensities, measured on spots 1, 2, and 3, as indicated in (a). (c) Stokes LFRS spectra of a series of twisted $MoSe_2$–WSe_2 heterobilayers. The twist angles, as determined from the moiré-phonon mode positions (see text), are indicated. (d) Comparison of the moiré-phonon mode positions to the calculated LA and TA phonon dispersion curves of monolayer $MoSe_2$ and WSe_2. The experimental data from the spectra in (c) is marked by diamonds of the same color. The average uncertainty of the twist angle across the heterostructure region, resulting from SHG determination, is indicated by a black double arrow (see text for explanation).

the ISM and BM [41]. The mode positions, which are unique for a given twist angle, are marked by small red and blue arrows. Red arrows mark the folded longitudinal acoustic modes, while folded transverse acoustic modes are marked by blue arrows. Figure 1(e) shows a comparison of the mode positions to calculations of the dispersions of longitudinal (LA) and transverse (TA) acoustic phonon branches for a $MoSe_2$ monolayer. The calculations are performed, following [52]. For the solid lines in figure 1(e), the calculated phonon dispersions for the $\Gamma-K$ and the $\Gamma-M$ directions have been averaged along the dotted line in figure 1(b), as described in detail in the supplemental material of [43]. The experimental error is smaller than the symbol size in figure 1(e). One can recognize good agreement of the experimental data with the calculated dispersion curves. Similar agreement has been observed for MoS_2 and WSe_2 homobilayers in [43] and [44], respectively. We complete this here for $MoSe_2$ homobilayers and take this as an overall good indication that the twist angles can be accurately determined via comparison of locally-observed moiré phonon energies to calculated monolayer phonon dispersion curves.

Next, we will discuss the LFRS results on the $MoSe_2$–WSe_2 *hetero*bilayers. Since for the preparation of heterobilayers the tear-and-stack technique can not be applied, the twist angle is not known from the preparation process as accurately as for homobilayers. Here, typically one has to rely on SHG measurements. An intrinsic drawback of this method for heterostructures is, however, that the SHG measurements have to be done on the monolayer parts of the individual layers, i.e. outside the bilayer region. In the following we will show that this comes with some uncertainties, in particular for large-area samples. We note that via phase-sensitive SHG measurements on the bilayer region, one can only discriminate between R-type and H-type stackings [23] but not accurately determine other twist angles. In the SHG experiments, the crystallographic orientation of the individual monolayers is determined by measuring the angle-resolved intensity of the polarized SHG signal. Figure 2(a) shows a microscope image of a large-area heterobilayer, investigated in this work. For this sample, a twist angle of $\theta = 60°$ (H-type) was intended. Three exemplary spots, where SHG measurements of the monolayers are taken, are labeled by stars, which are numbered by 1, 2, and 3 in figure 2(a) (in total, eight spots are measured on this sample). Figure 2(b) shows polar plots of the normalized SHG intensities, measured on these spots.

While the accuracy of the crystal orientation determination from a SHG measurement itself is about 1°, an uncertainty for the twist angle across the heterobilayer region is obvious from the results in figure 2(b): when comparing the measured orientations at spots 1 and 3, a twist angle $|\delta_1| \sim 5°$ can be deduced, while spots 2 and 3 deliver a value of $|\delta_2| \sim 3°$ for the relative twist angle of the two layers. We have measured the twist angles of in total 33 heterobilayers, where multiple spots could be measured, by this method and carefully analyzed the uncertainties for all individual samples. As a result of these investigations, taking into account all possible error sources, we receive an average uncertainty of about 4° for the twist angle of a heterostructure, as determined via SHG measurements on monolayer regions. This average uncertainty, which is corroborated by our local LFRS measurements further below, is indicated in figure 2(d).

Figure 2(c) shows Stokes LFRS spectra of four heterobilayers with different twist angles, as indicated in the figure. The black arrows mark peaks, which we assign to moiré phonons of the heterobilayers. On 12 samples out of a total of 33 prepared heterobilayers we could unambiguously identify two to four moiré modes from folded acoustic phonons, which could be reproducibly observed on different spots on the sample. The experimental mode positions are plotted in figure 2(d), where different colors correspond to different samples to emphasize the number of observed modes per sample. The data points, which are extracted from the spectra in figure 2(c), are indicated with diamonds in figure 2(d). As elaborated above, the twist angles as determined by SHG have a significant uncertainty. Therefore, we apply the following procedure to get a more precise twist-angle determination: The experimental data points in figure 2(d) are horizontally shifted within the twist-angle error margins of the individual SHG measurements for a best fit to the calculated $MoSe_2$ and WSe_2 monolayer phonon dispersions, plotted as solid lines in figure 2(d). Since the relative lattice mismatch between $MoSe_2$ and WSe_2 is only 0.004, we use here for the calculated curves the twist angles of the respective twisted homobilayers. Remarkably, for all samples a very good fit of the experimental mode positions to the calculated curves can be obtained, as mentioned, within the error bars of the SHG angle determinations. The average uncertainty of the SHG determination is exemplarily shown by the black double arrow in figure 2(d). For most of the samples we observe two moiré phonons of the $MoSe_2$ layer, only, which is the bottom layer of the heterostructure. For three samples, three moiré phonons are observed: two from $MoSe_2$ and one from WSe_2, and for one sample, we find all four moiré modes of the two materials (four red dots in figure 2(d) at 5.3°). Therefore, in the remainder we will concentrate on this sample (shown in the micrograph in figure 2(a)), which allows for a very accurate relative determination of the local twist angle because of four modes, which have to fit to the calculated dispersion curves. We emphasize here that there may still be an uncertainty in the *absolute* value of the twist angles because of the limited accuracy of DFT calculations. However, the *relative* twist angle between two samples, or, between different spots of the same sample, can be determined with high precision (see below).

We start by comparing LFRS spectra and low-temperature μPL on selected spots on this large-area heterobilayer. This H-type heterobilayer has a twist-angle deviation of $|\delta| = (5 \pm 3)°$ as determined via angle-resolved SHG from the monolayer regions (see above). Therefore, refering to the results of [51], we can expect some spatial regions with $|\delta| < 4°$, i.e. with atomic reconstruction of H-type in this sample. Figures 3(a) and (b) show room-temperature Stokes/antistokes LFRS spectra with unpolarized detection, taken in the regions, marked by a green circle and a yellow hexagon in figure 3(c), respectively. The two spectra are apparently markedly different. While the spectra in figure 3(a) show peaks, which can be assigned to moiré modes of the two layers (red and blue arrows corresponding to $MoSe_2$ and WSe_2 modes, respectively), the spectra in figure 3(b) exhibit only one sharp mode, which can be attributed to the ISM of the heterobilayer [51]. The observation of an ISM is a clear indication for atomic reconstruction [51], i.e. a relative twist angle of $\delta = 0$, while the observation of moiré phonons indicates a finite twist angle. In [51] it was shown that for $MoSe_2$–WSe_2 heterobilayers atomic reconstruction should be present for $|\delta| < 4°$. Therefore, we conclude that in the area, marked by the yellow hexagon in figure 3(c), the nominal twist angle must be in this range, and atomic reconstruction has taken place. This is strongly corroborated by low-temperature μPL measurements of the same sample region. Figure 3(e) exhibits a strong interlayer-exciton signal in the yellow-shaded region. Obviously, due to the atomic reconstruction, the lattices are perfectly matched on the atomic scale, and the interlayer-exciton transition is momentum-allowed and therefore bright. In figure 3(d), the PL from the region, marked with a green circle in figure 3(c), is plotted. There, no significant interlayer-exciton signal can be detected in the yellow-shaded region, while the intralayer PL signals of the constituent layers, around 1600 meV, are still present. With the finite twist-angle deviation of $|\delta| \sim 5°$, as deduced from the moiré-phonon energies, the interlayer-exciton is momentum forbidden, and therefore dark. This impressively demonstrates the strength of our method: Via LFRS experiments, the relative twist angle can be very accurately determined on a local scale. This allows one to distinguish between regions of atomic reconstruction and regions with a moiré lattice, i.e. a finite twist-angle deviation δ. To emphasize the accuracy, figure 3(f) shows a

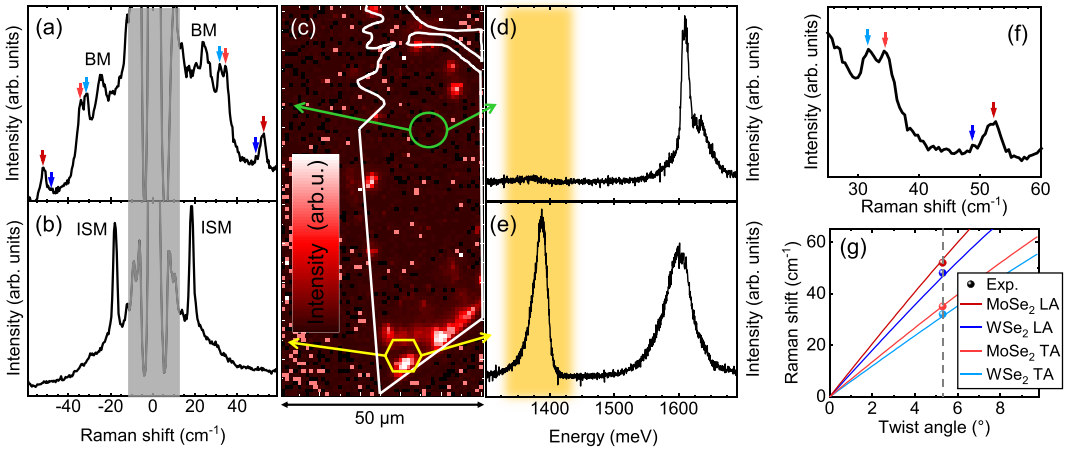

Figure 3. (a) Stokes/antistokes LFRS spectra from the region, indicated by a green circle in (c). The arrows mark positions of moiré phonons, BM labels the breathing mode of the bilayer. (b) Stokes/antistokes LFRS spectra from the region inside the yellow hexagon in (c). An interlayer shear mode ISM can be observed in this region. (c) Color map of low-temperature μPL intensities in the spectral region of the interlayer exciton, around 1390 meV. (d) PL spectrum from the region, marked with a green circle in (c). (e) PL spectrum from the region, marked with a yellow hexagon in (c). The yellow-shaded region highlights the interlayer exciton. (f) Enlargement of the Stokes spectrum in (a). (g) Comparison of the mode positions of the moiré phonons to the calculated LA and TA phonon dispersions of the monolayers. The vertical dotted line indicates the best fit, which yields a twist angle of 5.3°.

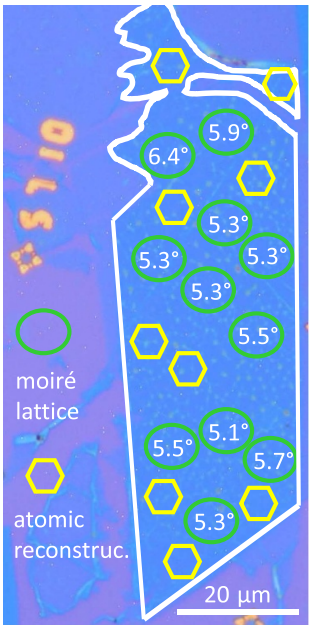

Figure 4. Microscope image of the heterobilayer sample, displayed in figure 2(a). The yellow hexagons mark regions, where a strong ISM is detected, i.e. which are atomically reconstructed. Regions where moiré phonons are measured, are indicated by green circles. The numbers give the local twist angles, as determined from the moiré phonon mode positions. A local variation of about 1° can be deduced for the twisted regions. For each region, the given twist angles are confirmed by measuring two to five different spots within the region.

blowup of the Stokes LFRS spectrum in figure 3(a). We note that the mode at ~ 49 cm^{-1} is only barely visible. It is, however, also present in the antistokes spectrum, and more pronounced in spectra on different sample spots, where the lower-energy peaks are then less pronounced. The experimental mode positions, as marked by arrows, are plotted in figure 3(g) together with the calculated acoustic phonon dispersions in this range. A best fit of the mode positions to the calculated curves delivers a twist angle of $|\delta| = 5.3°$, indicated by the vertical dashed line in figure 3(g). From this we estimate that a relative difference of twist angles of $\sim 0.1°$ can be detected by this method.

Finally, we show in figure 4 again a microscope image of the investigated heterobilayer. In this figure, regions which could be identified to be atomically reconstructed by the detection of a strong ISM signal, are marked by yellow hexagons, while regions, where moiré phonons could be detected, are marked with green circles. In these regions, the corresponding twist angles, as determined from the moiré-mode positions, are given. A twist-angle variation of about 1° can be noticed for the twisted regions. This is in overall good agreement with results on WSe_2 homobilayers [44] and our experiments on $MoSe_2$ homobilayers (not shown).

4. Conclusion

We have observed folded acoustic phonons of the moiré superlattice in twisted $MoSe_2$ homo- and $MoSe_2$–WSe_2 heterobilayers via low-frequency Raman spectroscopy. Comparison of the observed moiré phonon modes to calculations of the acoustic phonon dispersions of the constituent monolayers allows for a precise local twist-angle determination

of the heterobilayers. For a large-area heterobilayer, we have demonstrated the correlation between the intensity of an interlayer exciton at low temperatures with the corresponding room-temperature LFRS spectra: Spatial regions, which can be identified to have atomic reconstruction by the observation of a strong interlayer shear mode in the LFRS experiments, show a strong and sharp momentum-allowed interlayer exciton signal, while regions, where moiré phonons can be detected, exhibit no significant interlayer-exciton signal. This demonstrates that room-temperature LFRS of interlayer shear modes and moiré phonons is a highly valuable tool for the identification of spatial regions in transition-metal dichalcogenide heterostructures where, e.g. interesting moiré physics, like correlated interlayer-exciton phases, can be expected in high-quality samples.

Data availability statement

The data that support the findings of this study are available upon reasonable request from the authors.

Acknowledgments

We greatfully acknowledge funding by the Deutsche Forschungsgemeinschaft (DFG, German Research Foundation) - Project-ID 314695032-SFB 1277 (subproject B05), SPP2244, and projects KO3612/3-1, KO3612/4-1, and SCHU1171/10-1.

ORCID iDs

Philipp Parzefall https://orcid.org/0000-0001-5015-329X
Johannes Holler https://orcid.org/0000-0002-5271-5265
Kai-Qiang Lin https://orcid.org/0000-0001-9609-749X
Bo Peng https://orcid.org/0000-0001-6406-663X
Bartomeu Monserrat https://orcid.org/0000-0002-4233-4071
Tobias Korn https://orcid.org/0000-0003-4808-391X
Christian Schüller https://orcid.org/0000-0002-6043-5263

References

[1] Geim A K and Grigorieva I V 2013 *Nature* **499** 419
[2] Cao Y, Fatemi V V, Fang S, Watanabe K, Taniguchi T, Kaxiras E and Jarillo-Herrero P 2018 *Nature* **556** 43
[3] Koperski M, Molas M R, Arora A, Nogajewski K, Slobodeniuk A O, Faugeras C and Potemski M 2017 *Nanophotonics* **6** 1289
[4] Wang G, Chernikov A, Glazov M M, Heinz T F, Marie X, Amand T and Urbaszek B 2018 *Rev. Mod. Phys.* **90** 21001
[5] Mak K F, Lee C, Hone J, Shan J and Heinz T F 2010 *Phys. Rev. Lett.* **105** 136805
[6] Chernikov A, Berkelbach T C, Hill H M, Rigosi A F, Li Y, Aslan O B, Reichman D R, Hybertsen M S and Heinz T F 2014 *Phys. Rev. Lett.* **133** 076802
[7] Poellmann C *et al* 2015 *Nat. Mater.* **14** 889
[8] Xiao D, Liu G B, Feng W, Xu X and Yao W 2012 *Phys. Rev. Lett.* **108** 196802
[9] Mak K F, He K, Shan J and Heinz T F 2012 *Nat. Nanotechnol.* **7** 494
[10] özçelik V O, Azadani J G, Yang C, Koester S J and Low T 2016 *Phys. Rev.* B **94** 035125
[11] Kośmider K and Fernández-Rossier J 2013 *Phys. Rev.* B **87** 075451
[12] Kang J, Tongay S, Zhou J, Li J and Wu J 2013 *Appl. Phys. Lett.* **102** 012111
[13] Fang H *et al* 2014 *Proc. Natl Acad. Sci.* **111** 6198
[14] Rivera P *et al* 2015 *Nat. Commun.* **6** 6242
[15] Rivera P, Seyler K L, Yu H, Schaibley J R, Yan J, Mandrus D G, Yao W and Xu X 2016 *Science* **351** 688
[16] Kunstmann J *et al* 2018 *Nat. Phys.* **14** 801
[17] Nayak P K *et al* 2017 *ACS Nano* **11** 4041
[18] Zhang C, Chuu C P, Ren X, Li M Y, Li L, Jin C, Chou M Y and Shih C K 2017 *Sci. Adv.* **3** e1601459
[19] van der Zande A M *et al* 2014 *Nano Lett.* **14** 3869
[20] Alexeev E M *et al* 2019 *Nature* **567** 81
[21] Jin C *et al* 2019 *Nature* **567** 76
[22] Seyler K L, Rivera P, Yu H, Wilson N P, Ray E L, Mandrus D G, Yan J, Yao W and Xu X 2019 *Nature* **567** 19
[23] Tran K *et al* 2019 *Nature* **567** 71
[24] Brotons-Gisbert M *et al* 2020 *Nat. Mater.* **19** 630
[25] Brotons-Gisbert M, Baek H, Campbell A, Watanabe K, Taniguchi T and Gerardot B D 2021 (arXiv:2101.07747v1)
[26] Bistritzer R and MacDonald A H 2011 *Proc. Natl Acad. Sci.* **108** 12233
[27] Cao Y *et al* 2018 *Nature* **556** 80
[28] Wang L *et al* 2020 *Nat. Mater.* **19** 861
[29] Cao Y, Rodan-Legrain D, Rubies-Bigorda O, Park J M, Watanabe K, Taniguchi T and Jarillo-Herrero P 2020 *Nature* **583** 215
[30] Liu X *et al* 2020 *Nature* **583** 221
[31] Mait I, Naik M H, Maiti P K, Krishnamurthy H R and Jain M 2020 *Phys. Rev. Res.* **2** 013335
[32] Kumar H, Er D, Dong L, Li J and Shenoy V B 2015 *Sci. Rep.* **5** 10872
[33] Rosenberger M R, Chuang H J, Phillips M, Oleshko V P, McCreary K M, Sivaram S V, Hellberg C S and Jonker B T 2020 *ACS Nano* **14** 4550
[34] Weston A *et al* 2020 *Nat. Nanotechnol.* **15** 592
[35] Sushko A, De Greve K, Andersen T I, Scuri G, Zhou Y, Sung J, Watanabe K, Taniguchi T, Kim P, Park H and Lukin M D (arXiv:1912.07446)
[36] Carr S, Massatt D, Torrisi S B, Cazeaux P, Luskin M and Kaxiras E 2018 *Phys. Rev.* B **98** 224102
[37] Wozniak T, Faria Junior P E, Seifert G, Chaves A and Kunstmann J 2020 *Phys. Rev.* B **101** 235408
[38] Enaldiev V V, Zolyomi V, Yelgel C, Magorrian S J and Fal'ko V I 2020 *Phys. Rev. Lett.* **124** 206101
[39] Ferrari A and Basko D 2013 *Nat. Nanotechnol.* **8** 235
[40] Zhang X, Qiao X F, Shi W, Wu J B, Jiang D S and Tan P H 2015 *Chem. Soc. Rev.* **44** 2757
[41] Liang L, Zhang J, Sumpter B G, Tan Q H, Tan P H and Meunier V 2017 *ACS Nano* **11** 11777
[42] Tan P H (ed) 2019 *Raman Spectroscopy of Two-Dimensional Materials* (*Springer Series in Materials Science*) (Singapore: Springer Nature)
[43] Lin M L *et al* 2018 *ACS Nano* **12** 8770
[44] Lin K Q, Holler J, Bauer J M, Scheuck M, Peng B, Korn T, Bange S, Lupton J M and Schüller C 2020 (arXiv:2012.13820)
[45] Liang L, Puretzky A A, Sumpter B G and Meunier V 2017 *Nanoscale* **40** 15340
[46] Plechinger G, Heydrich S, Eroms J, Weiss D, Schüller C and Korn T 2012 *Appl. Phys. Lett.* **101** 101906
[47] Lui C H *et al* 2015 *Phys. Rev.* B **91** 165403

[48] Puretzky A A, Liang L, Li X, Xiao K, Sumpter B G, Meunier V and Geohegan D B 2016 *ACS Nano* **10** 2736
[49] Lin M L, Zhou Y, Wu J B, Cong X, Liu X L, Zhang J, Li H, Yao W and Tan P H 2019 *Nat. Commun.* **10** 2419
[50] Okada M *et al* 2018 *ACS Nano* **12** 2498
[51] Holler J, Meier S, Kempf M, Nagler P, Watanabe K, Taniguchi T, Korn T and Schüller C 2020 *Appl. Phys. Lett.* **117** 013104
[52] Peng B, Zhang H, Shaob H, Xua Y, Zhanga X and Zhu H 2016 *RSC Adv.* **6** 5767
[53] Castellanos-Gomez A, Buscema M, Molenaar R, Singh V, Janssen L, van der Zant H S J and Steele G A 2014 *2D Materials* **1** 011002
[54] Kim K *et al* 2016 *Nano Lett.* **16** 1989
[55] Li Y, Rao Y, Mak K F, You Y, Wang S, Dean C R and Heinz T F 2013 *Nano Lett.* **13** 3329
[56] Moon P and Koshino M 2013 *Phys. Rev.* B **87** 205404
[57] Lamparski M, Van Troeye B and Meunier V 2020 *2D Materials* **7** 025050
[58] Quan J *et al* 2021 *Nat. Mater.* (https://doi.org/10.1038/s41563-021-00960-1)